Observing the influence of the youngest super star clusters in NGC 1569: Keck Brackett α spectroscopy

Daniel P. Cohen,[1][*] Jean L. Turner,[1] Sara C. Beck,[2] S. Michelle Consiglio,[1]

[1]*Department of Physics and Astronomy, University of California, Los Angeles, CA 90095-1547, USA*
[2]*School of Physics and Astronomy, Tel Aviv University, Ramat Aviv, Israel*

ABSTRACT

We report Keck-NIRSPEC observations of the Brackett α 4.05 μm recombination line across the two candidate embedded super star clusters (SSCs) in NGC 1569. These SSCs power a bright H II region and have been previously detected as radio and mid-infrared sources. Supplemented with high resolution VLA mapping of the radio continuum along with IRTF-TEXES spectroscopy of the [S IV] 10.5μm line, the Brackett α spectra data provide new insight into the dynamical state of gas ionized by these forming massive clusters. NIR sources detected in 2μm images from the Slit-viewing Camera are matched with GAIA sources to obtain accurate celestial coordinates and slit positions to within $\sim 0\rlap{.}{''}1$. Br α is detected as a strong emission peak powered by the less luminous infrared source, MIR1 ($L_{\rm IR} \sim 2 \times 10^7$ L$_\odot$). The second candidate SSC MIR2 is more luminous ($L_{\rm IR} \gtrsim 4 \times 10^8$ L$_\odot$) but exhibits weak radio continuum and Br α emission, suggesting the ionized gas is extremely dense ($n_e \gtrsim 10^5$ cm^{-3}), corresponding to hypercompact H II regions around newborn massive stars. The Br α and [S IV] lines across the region are both remarkably symmetric and extremely narrow, with observed line widths $\Delta v \simeq 40$ km s^{-1}, FWHM. This result is the first clear evidence that feedback from NGC 1569's youngest giant clusters is currently incapable of rapid gas dispersal, consistent with the emerging theoretical paradigm in the formation of giant star clusters.

Key words: galaxies: individual: NGC 1569, galaxies: kinematics and dynamics, galaxies: starburst, galaxies: star clusters, galaxies: star formation, ISM: HII regions

1 INTRODUCTION

As the birth places for nearly all massive stars, giant star clusters fundamentally shape the dynamics and chemistry of their host galaxies. Galactic observations of ancient globular clusters (GCs) give a direct view into the evolved phase of massive star cluster evolution. These investigations have revealed unexpected properties of GCs that are determined entirely within their *earliest* evolutionary phase. Of particular interest are how massive clusters survive the first ~ 5 Myrs of intense feedback from massive stellar evolution and remain bound for Gyrs, and how they form the multiple stellar populations that are ubiquitous in GCs (e.g., Piotto et al. 2015; Bastian & Lardo 2018). The only young clusters with comparable masses exist within rare *extragalactic* starburst regions. Super star clusters (SSCs) host 10^5-10^6 M$_\odot$ in stars and gas and may represent directly observable analogs of proto-globular clusters (e.g., Turner 2009).

The youngest SSCs are still deeply embedded within their natal clouds of gas and dust and suffer large internal extinction, rendering them unobservable in optical-NIR wavelengths. However, these clusters ionize luminous compact H II regions that are detected as radio-IR "supernebulae". The dynamics of such supernebulae reflect the collective influence of rapidly evolving massive stars (Beck 2008), providing unparalleled insight into the mechanisms of retention or expulsion, hence survivability, of massive clusters like GCs (Elmegreen 2018; Gray et al. 2019). Requiring high spatial and spectral resolution in the IR/radio, direct measurements of supernebula kinematics have, until recently, been largely infeasible.

Observations of SSCs made within the last few years provide evidence for a fundamental difference in how feedback operates in the densest, most-massive star clusters. The supernebula in dwarf starburst galaxy NGC 5253 exhibits a recombination linewidth of merely $\Delta v \sim 75$ km s^{-1}, similar to linewidths of Galactic HII regions, despite being powered by a $M \sim 4 \times 10^5$ M$_\odot$ cluster with $\sim$2000 O stars

and hot molecular cores within its $r \sim 3$ pc extent (Turner et al. 2000; Meier et al. 2002; Turner et al. 2003; Turner & Beck 2004; Calzetti et al. 2015; Smith et al. 2016; Consiglio et al. 2017; Turner et al. 2017; Cohen et al. 2018; Silich et al. 2020). Simulations find that the most highly concentrated forming SSCs host ionized stellar wind regions that can stall in their expansion due to critical radiative cooling, preventing a coherent cluster wind and allowing the cluster to retain enriched fuel for ongoing star formation (Silich & Tenorio-Tagle 2018, 2017; Gray et al. 2019; Silich et al. 2020). Finding and studying more SSCs such as the NGC 5253 supernebula is critical to solving the unanswered questions of GC formation and galaxy evolution.

Perhaps the next best candidate of a proto-globular cluster after NGC 5253 is found within dwarf starburst NGC 1569, located at a distance of $D = 3.4$ Mpc (Grocholski et al. 2012) and known for its two bright, visible SSCs, A and B (e.g., Hunter et al. 2000). Currently NGC 1569's most active star formation is concentrated to an obscured region characterized by high extinction (Galliano et al. 2003; Pasquali et al. 2011; Lianou et al. 2014; Westcott et al. 2018). Intense thermal radio continuum coinciding with bright He I and Pa β emission indicates the presence of H II regions excited by forming massive star clusters (Greve et al. 2002; Clark et al. 2013). The brightest H II region, identified as H II 2 in Waller (1991), is located near a group of CO clouds at the end of a Hα filament extending ~ 2 kpc (Taylor et al. 1999). H I along this filament exhibits redshifted non-circular motion (Johnson et al. 2012), indicating a potential inflow into the embedded star-forming region. This could be an example of filament-fed star formation, much like the case suggested for NGC 5253 (Turner et al. 2015; Consiglio et al. 2017).

Two candidate embedded forming massive clusters in NGC 1569, identified with high resolution [S IV] 10.5 μm and mid-infrared continuum imaging in Tokura et al. (2006) as MIR1 and MIR2, may be the very youngest clusters in NGC 1569. They appear to be responsible for ionizing H II 2. Tokura et al. (2006) find that the brighter source MIR1 has an estimated intrinsic infrared luminosity on the order of 10^7 L$_\odot$, corresponding to $\gtrsim 100$ O7 stars (revised for $D = 3.4$ Mpc). Despite a weaker line flux, the second source MIR2 is estimated to have a higher intrinsic luminosity of $\gtrsim 10^8$ L$_\odot$. MIR2 should be easily detectable in the radio continuum, but exhibits no clear radio counterpart. The IR luminosity of MIR2 is consistent with ionization from thousands O7 stars. This suggests MIR2 is a SSC in the earliest phases of formation, where the density is so high that the nebula is optically thick in free-free emission and has a bright and hot dust continuum emission. MIR1 and MIR2 are separated by only 1.5″, or 30 pc in projection. Their relation along with their gas kinematics, is unclear.

In this paper we present the Br α emission line spectrum across embedded SSC candidates MIR1 and MIR2 and the brightest H II region in NGC 1569, obtained with the NIRSPEC echelle spectrograph on Keck. At 4 μm, the Br α line is less effected by extinction than Hα or Br γ. The NIRSPEC observations are complemented with high resolution VLA mapping of the 6 cm continuum along with high resolution spectroscopy of the [S IV] 10.5 μm line from the IRTF. For the first time, the spectra reveal the dynamical nature of the embedded ionized gas in the giant H II region at a ~ 10 km s^{-1} resolution. The adopted distance of of $D = 3.4$ Mpc for NGC 1569 (Grocholski et al. 2012) corresponds to a scale of 1″=16 pc.

2   OBSERVATIONS

2.1   Radio continuum with the VLA

Radio continuum maps were used to position the NIRSPEC slit on NGC 1569's embedded giant H II region complex and provide a powerful complement to the Br α spectroscopy. NGC 1569 was observed with the VLA in A configuration on 23 August 1999 at C (6 cm) band in program AT227 (P.I. J. Turner). Fluxes were calibrated using 3C286; the absolute flux calibration is estimated to be to better than 5%, although this does not include flux lost due to undersampling in these high resolution maps. The uvdata were tapered to give a beam of size 0.″78 × 0.″66 (FWHM) at P.A. = 71°. The shortest baseline is $\sim 10^4$ kλ, so structures of extent greater than $\sim 15''$ are poorly sampled. The rms in the map is 0.12 mJy/beam.

The 6 cm continuum map is shown in Fig. 1. In lower resolution maps by Lisenfeld et al. (2004) and Westcott et al. (2018), radio continuum emission is observed over a 2′ region centered on the visible SSCs in NGC 1569. The region mapped here is near their "H II 2" source, which is identified as radio source "M-1" in 1.4 GHz MERLIN maps of Greve et al. (2002). The radio continuum in this region is characterized by a flat spectral index (Greve et al. 2002; Lisenfeld et al. 2004; Westcott et al. 2018), consistent with thermal free-free emission. Extended emission in this smaller M-1 region is not well sampled by the high resolution VLA image. The total 6 cm flux for the region shown in the figure is roughly 20 mJy.

The compact radio source in Fig. 1 is source MIR1 identified by Tokura et al. (2006). A Gaussian fit to the 6 cm source gives a position for this radio source of R.A., Dec. (ICRS) = 04$^{\rm h}$30$^{\rm m}$46.$^{\rm s}$913±0.$^{\rm s}$007, 64°51′00.″57±0.″03, in good agreement with the 1.4 GHz MERLIN coordinates of Greve et al. (2002). The source appears to be slightly extended, with a peak flux of 1.3±0.1 mJy/beam and a total flux density of 1.9 mJy. The region corresponding to MIR2 has weak if any 6 cm continuum emission, and we put an upper limit of 0.3 mJy for a radio source at this location.

2.2   Br α spectroscopy with NIRSPEC

We observed the embedded star-forming region in NGC 1569 with NIRSPEC on Keck II (McLean et al. 1998) during the first half-night on Dec 7, 2017. Two high-resolution (echelle) spectra, each with 240s integration, were acquired in the KL band through a 0.″432×24″ slit positioned on the galaxy's thermal radio continuum peak and candidate embedded SSCs MIR1 and MIR2, as shown in Figure 2. The echelle and cross-disperser angles were set to 64.42° and 34.3°, respectively, to observe the Br α line in the 19th echelle order. The resulting wavelength coverage of this order was 4.032-4.085 μm. The calibration star, HD12365, was observed with an ABBA nod sequence prior to observations of NGC 1569. Each slit position yielded a 2D echelle spectrum which
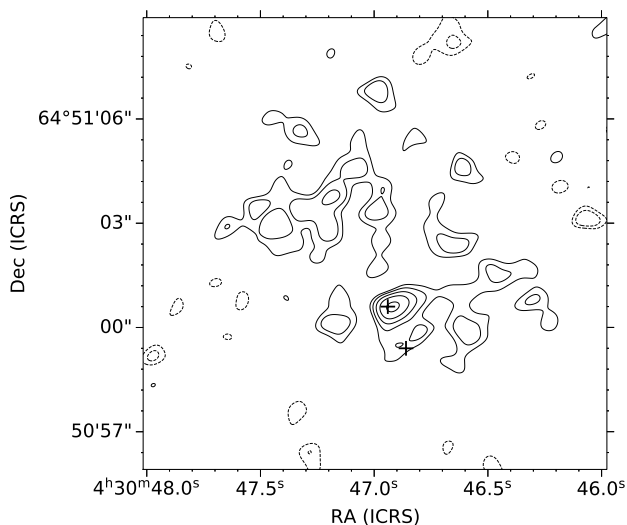
Figure 1. VLA map of the 6cm radio continuum near the embedded H II complex in NGC 1569. Contours are drawn at brightness levels 0.25 mJy/beam $\times\, 2^{n/2}$ for $n = \{0, 1, 2, 3, 4, 5, 6, 7, 8\}$, and dashed contours mark negative levels $n = \{0, 1, 3, 4\}$. The peak brightness is 1.0911 mJy/beam. Crosshairs mark the positions of MIR1 and MIR2 from Tokura et al. (2006), who assumed MIR1 is coincident with the radio peak; these sources are also marked in Fig. 2.

we rectified and reduced. Reduction involved the use of flat-field and ThArXeNe arc-lamp spectra acquired at the beginning of the night, and a raw sky spectrum taken after NGC 1569 exposures at an offset of $\sim 50''$. After first being cleaned of cosmic rays and bad pixels, raw science spectra were sky-subtracted (or $A - B$ subtracted in the case of HD12365) and divided by a median-normalized flat-field image. The spectra were then rectified – mapped from the curved echelle order onto a grid with orthogonal spatial and dispersion axes, using transformations generated with the SPATMAP and SPECMAP routines from the REDSPEC reduction code[1]. The wavelength calibration was determined as part of the SPECMAP procedure by identifying arc-lamp lines and fitting their positions with a 3rd-order polynomial.

Figure 3 shows the combined reduced echelle spectrum, along with the spatial profile of the Brackett α emission. The echellegram has spatial information along the vertical axis and spectral information along the horizontal axis, with a pixels size of $0.''152$ by 5.44×10^{-5} μm. The instrumental spectral resolution at 4.051 μm is 12 km s^{-1}. The Br α line profiles of identified sources, reported in Figure 4, are extracted from the echelle spectrum by collapsing along the spatial axis within apertures of size determined by source size. The photometric calibration was estimated with the spectrum of HD12365 by summing the star's spectral trace and adopting a 65% flux loss by the $0.''5$ slit, allowing us to convert measured flux in counts s^{-1} to physical units. Wavelengths and velocities quoted in this paper have been converted to the heliocentric frame.

[1] https://www2.keck.hawaii.edu/inst/nirspec/redspec.html

2.3 [S IV] spectroscopy with TEXES

The [S IV] 10.5 μm line was observed across NGC 1569's radio cotinuum/MIR peak with TEXES (Lacy et al. 2002) on the NASA IRTF on Jan 1, 2012. The [SIV] line is excited by hot stars of more than ~ 40 $M_\odot$. It is affected by extinction approximately as much as is the Br α and is less susceptible to thermal broadening. The $29''$ slit was oriented north-south and centered on the position of MIR1 using blind-offset pointing from a guide star. Additional spectra were acquired by stepping the slit $0.''7$ east/west (half the seeing FWHM $1.''4$). The instrumental resolution for the spectra (medium resolution mode) is ~ 18 km s^{-1}. The [S IV] line profile observed at the central pointing is shown in Fig. 5 and discussed further in Sec. 3.2.

3 RESULTS

3.1 Relating radio continuum and Br α to MIR sources

Imaging of the KL-band continuum, which for simplicity we also refer to as "2μm" continuum, was obtained with the NIRSPEC Slit-Viewing Camera (SCAM) during spectral exposures and used to determine accurate positioning of the slits on the sky (Fig. 6). To perform astrometric calibration, we first combined sky-subtracted SCAM images for each of the two on-target positions, and measured the pixel positions of bright IR sources detected within each image. The IR sources were then matched to sources with well-established ICRS coordinates from the Gaia DR2 catalog (Gaia Collaboration et al. 2016, 2018), as marked in Fig. 6. Residuals of the best-fit astrometric solutions are $\sim 0.''1$ (RMS).

The SCAM imaging indicates a seeing FWHM of $0.''8 \simeq$ 13 pc, which should be capable of resolving separate continuum emission peaks from MIR1 and MIR2, which are separated by $1.''5$. MIR1 indeed coincides with a local peak in the KL continuum, but one that is fainter than continuum to its east and especially near cluster #10 to the NE (the brightest KL-band peak in Fig. 2, right). Moreover MIR2, despite its bright 10μm continuum, has no clear KL-band counterpart. Radio continuum is detected at MIR2 as a southern extension with no clearly detected source. Considering that MIR2 is the brightest 10μm continuum sources in NGC 1569, its lack of both radio and NIR continuum emission suggests suggests that it hosts extremely dense H II regions and could be in a very early phase of formation, as proposed by Tokura et al. (2006).

The morphology of Br α emission is illustrated by the echelle spectrum and intensity profile in Fig. 3. The brightest Br α source is identified as "Br-MIR1" because of its clear association with the compact MIR sources. Br-MIR1 encompasses a sharp peak at the location of MIR1 and prominent shoulder of emission extending $\sim 2''$ to its south, past the expected position of MIR2. The size of Br-MIR1, calculated from a single Gaussian fit to its intensity profile, is $\Delta\theta_{\mathrm{FWHM}} \simeq 2.''2 \simeq 35$ projected-pc. Given the $\sim 1.''5$ separation between MIR1 and MIR2, any detectable emission from MIR2 should be resolved by NIRSPEC. Rather, Br-MIR1 exhibits only the peak at MIR1, suggesting faint or negligible Br α emission from MIR2. This structure appears to closely follow the radio continuum (Fig. 1). Despite no
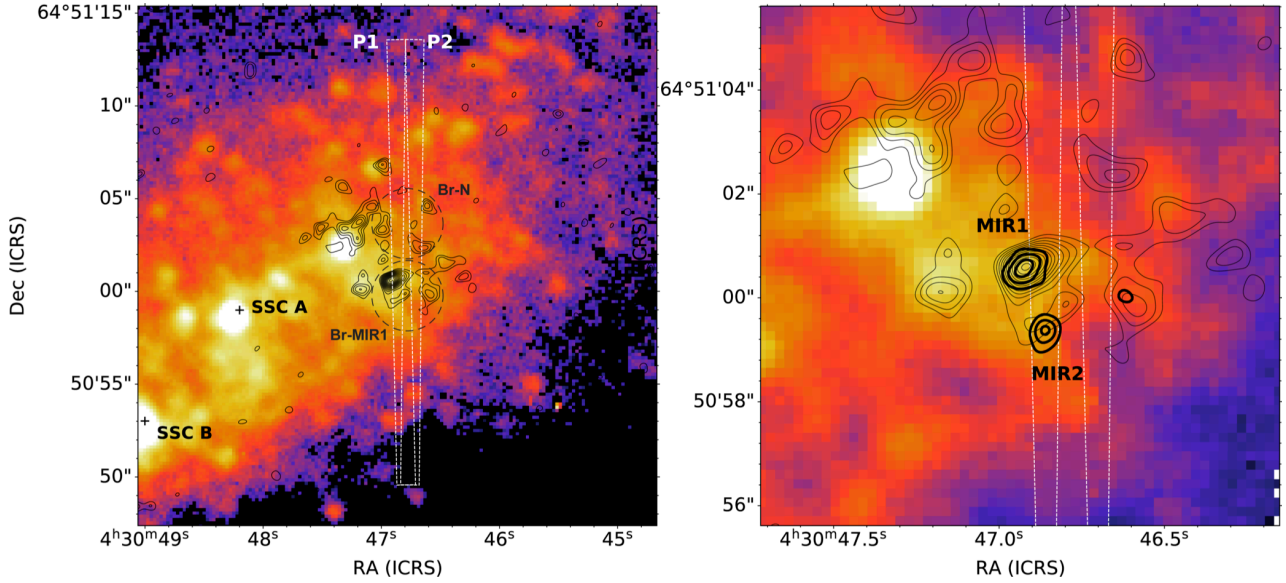
Figure 2. NIRSPEC observations of the embedded star-forming region in NGC 1569. *Left*) Positions of the $0\rlap{.}''432 \times 24''$ slits (white boxes) over the combined SCAM image of the KL-band continuum (colorscale). Slits were centered near the bright thermal radio continuum/MIR peak (Fig. 1). The approximate locations of the two brightest Brα emission peaks Br-N and Br-MIR1 (Sec. 3.1 and Fig. 3) are marked by the black dashed circles. Optical SSCs A and B are shown for reference. *Right*) Zoom-in of target region, showing the relation between 10μm continuum (thick contours; Tokura et al. 2006), radio continuum (thin contours), and KL-band (colorscale). MIR1 and MIR2 stand out as the brightest MIR sources in the region by far. The seeing measured in the SCAM imaging is roughly $1'' \simeq 16$ pc.
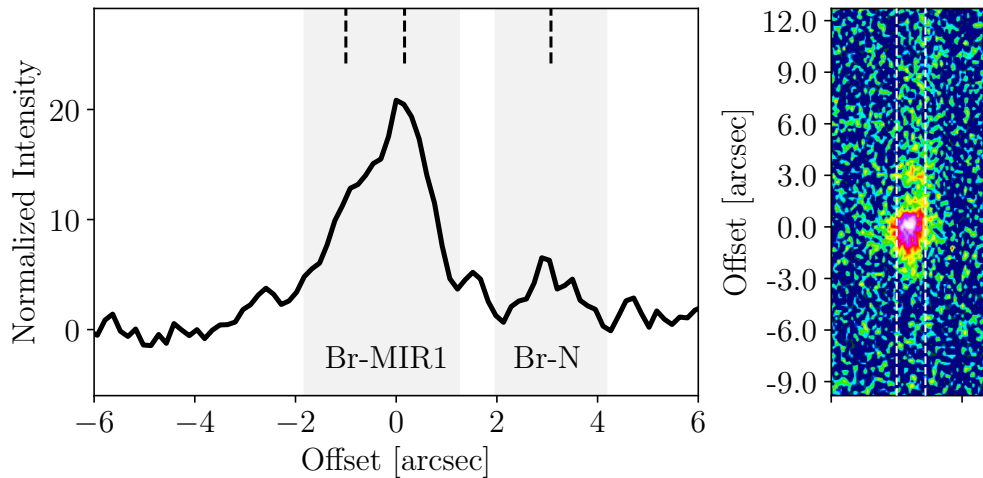

Figure 3. The combined 2D echelle spectrum of Brα from NIRSPEC (right) and the extracted intensity profile along the slit (left). In the echelle spectrum, the spectral and spatial axes are along x and y, respectively. The 1D spatial profile was extracted from the spectrum by averaging columns between the white dashed lines. Grey bands identify the strongest Brα emission sources: (1) Br-MIR1 encompassing the target H II region complex and MIR sources, and (2) an unrelated source Br-N located $3''$ to its north. Dashed vertical lines mark best-fit peak positions (Br-MIR1 is fit with two blended components).

clear signal from MIR2, the shoulder extending from MIR1 to MIR2 presents a potential physical link between the two sources.

The second Brα source identified in Fig. 3, Br-N, is located $3''$ to the north of Br-MIR1 and has best-fit size $\Delta\theta_{\rm FWHM} \simeq 1\rlap{.}''2 \simeq 20$ projected-pc. Br-N has no relation to MIR2 nor MIR1 but could be linked to the radio emission near cluster #10 from Westmoquette et al. (2007). Further north, Brα emission is tentatively in narrow peaks up to

$\sim 8''$ past Br-MIR1. These fluctuations could trace density enhancements like filaments intersecting the slit or possibly thin shells of ionized gas like those observed around many H II regions (Sewilo et al. 2004b).

3.2 Ionized Gas Kinematics

Kinematic properties were measured from the spectra extracted for Br-MIR1 and Br-N with apertures of radius
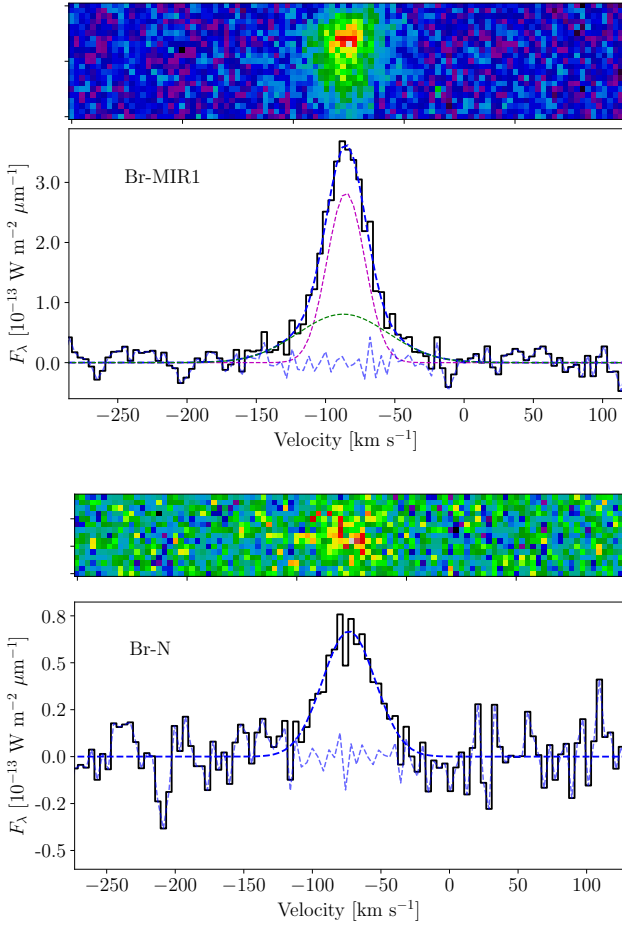
Figure 4. Br α line profiles of sources Br-MIR1 (top) and Br-N (bottom) identified in Fig. 3, extracted by summing the rows in the 2D spectra (colorscale). Br-MIR1 and Br-N are detected with peak S/N ratios of $\sim$30 and 8, respectively. Dark and light blue dashed curves show the best-fit profiles and residuals. Two Gaussian components are fit to Br-MIR1 (magenta and green dashed curves), while Br-N is fit with a single Gaussian profile.
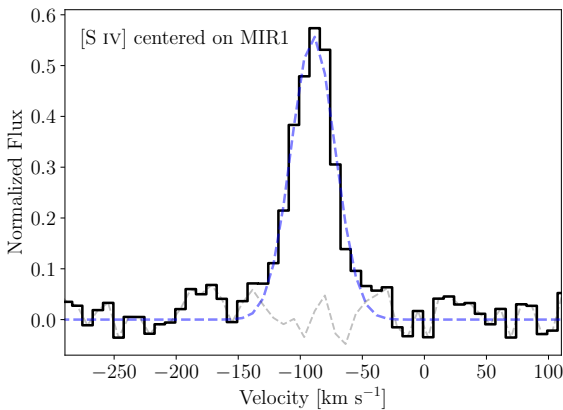

Figure 5. [S IV] 10.5 μm line observed with TEXES at the position of the compact radio peak/MIR1 (black curve), along with the best-fit Gaussian profile and residuals (blue and grey dashed curves, respectively).
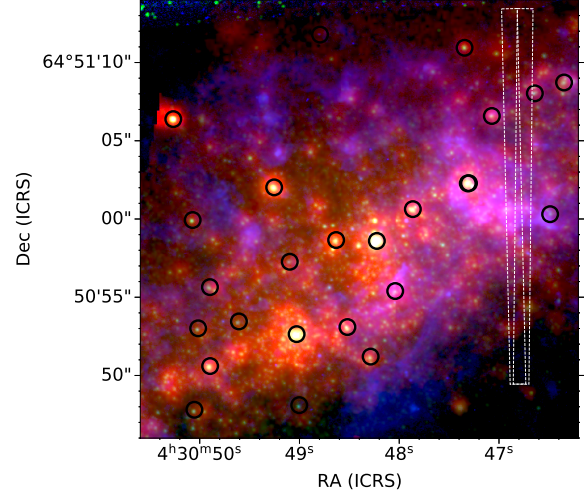

Figure 6. Registration of the slits (white boxes) with GAIA sources (black circles). The background three-color image shows archival HST F656N (blue) and F814W (green) along with the KL-band (red). The astrometric solution is accurate to $\sim 0''.1$

$r = 7\text{pix} \simeq 1''.1$ (Fig. 4). The Br α lines from both sources appear remarkably symmetric; $\chi^2_\nu = 1.6$ and 1.2 for a best-fit Gaussian profile to the spectrum of Br-MIR1 and Br-N, respectively. A two-component Gaussian profile provides a better model for Br-MIR1, however, to account for its broad wings ($\chi^2_\nu = 1.3$; Fig. 4). The measured properties of the Br α line, including both the single-component and two-component fit of Br-MIR1, are reported in Table 1.

Br-MIR1 exhibits an extremely narrow line profile, only $\Delta V_{\text{FHWM}} = 42 \pm 2$ km s^{-1}. This result in confirmed by the [S IV] spectrum from TEXES, shown with its best-fit single Gaussian profile in Fig. 5 ($\chi^2_\nu = 0.87$). Like Br α, the [S IV] line is symmetric and narrow, with a best-fit line width $\Delta V_{\text{[SIV]}} = 41 \pm 2$. The centroid velocities of Br α and [S IV] are coincident to within $\lesssim 5$ km s^{-1} (-85 ± 1 km s^{-1} and -89 ± 4 km s^{-1}, respectively), suggesting both lines originate in the same gas. Taken together, the results leave little doubt of the quiescent nature of ionized gas across Br-MIR1, NGC 1569's giant embedded star forming region.

3.2.1 Two-component Structure

The Br α emission from Br-MIR1 exhibits two velocity components: a narrow core with line width (FWHM) $\Delta V_n = 32 \pm 3$ km s^{-1} and a broader pedestal with $\Delta V_b = 74 \pm 12$. Each component contributes $\sim$50% of the total line flux. A narrow+broad Br α line profile is common for embedded SSCs, however such massive clusters are often observed to have broad-component line widths of $\Delta V_b \sim 250 - 350$ km s^{-1}(Henry et al. 2007; Beck 2008; Cohen et al. 2018), much larger than that of Br-MIR1. For comparison, the embedded supernebula in NGC 5253 exhibits a *narrow* component line width $\Delta V_n \sim 75$ km s^{-1} (Cohen et al. 2018). The line profile of Br-MIR1 is perhaps most comparable to Galactic hypercompact H II regions, which have typical linewidths of 30-50 km s^{-1}(e.g., Hoare et al. 2007; Sewilo et al. 2004a). We note that the broad component does not

appear on the [S IV] line in Fig. 5, possibly a reflection of nebular excitation structure.

3.2.2 North-South Variation

The centroid velocity of Br-MIR1 is consistent with the stellar and H I gas systemic velocities for NGC 1569 (Johnson et al. 2012), but shifts towards higher velocity to the north of Br-MIR1, with $V_{\rm hel} = -72$ km s^{-1} measured for Br-N. The implied gradient is roughly $+5$ km s^{-1} arcsec^{-1} or 0.3 km s^{-1} pc^{-1} from south to north.

The spatial dependence of centroid velocity and line width along the north-south slit axis is investigated further by extracting 1D spectra from non-overlapping 4 pixel-wide ($0\rlap{.}''6$) apertures along the spatial axis of the 2D spectrum and fitting the line with single-component Gaussian profiles. A change in the line shape and peak position is visible by eye in the observed spectra in Fig. 7, left. Best-fit $V_{\rm hel}$ and ΔV are shown as a function of offset in Fig. 7, right, revealing this pattern in more detail. A positive velocity gradient of $\simeq 2$ km s^{-1} arcsec^{-1} extends to the south of the peak of Br-MIR1, along its shoulder. The slight redshift south along the shoulder corresponds to a sharp decrease in line width from ~ 45 km s^{-1} at the peak to ~ 30 km s^{-1} at an offset of $-2''$.

A much steeper positive gradient of ~ 10 km s^{-1} arcsec^{-1} in velocity centroid occurs to the north of Br-MIR1, where it reaches a maximum $V_{\rm hel} \simeq -65$ km s^{-1} at an offset of just over $+2''$, and then reversing sign and decreasing until the location of Br-N where $V_{\rm helio} \simeq -75$ km s^{-1}. The minimum velocity centroid seemingly corresponds to a local maximum in the line width of 45 km s^{-1}.

4 DISCUSSION: PROPERTIES OF THE EMBEDDED CLUSTERS

The sources MIR1 and MIR2 discovered in the high resolution mid-infrared imaging of Tokura et al. (2006) are the first indications of the presence of heavily embedded young SSCs in the region, among the very youngest known. Informed by lower resolution investigations of the host region, we can use our high-resolution VLA radio continuum data, along with our Br α fluxes and linewidths, to improve on the analysis done by Tokura et al. and characterize the H II region that these two sources represent.

4.1 The host star-forming region

Much of our current understanding of the MIR sources is based on lower resolution mapping across their host region. In the radio, the region corresponds to a bright concentration of thermal free-free continuum powered by thousands of newborn massive stars (e.g., Lisenfeld et al. 2004; Westcott et al. 2018; Hindson et al. 2018). The 6 cm maps from Lisenfeld et al. (2004) and Westcott et al. (2018) indicate a peak brightness of ~ 10 mJy per $6''$ beam, with $\gtrsim 60\%$ of the emission being thermal. This number is comparable to the total observed flux of 2-3 mJy for MIR1 and MIR2 from the high resolution VLA data (Fig. 1), suggesting these sources contribute the bulk of ionization of the region.

In addition to its bright radio continuum, the H II 2 region is associated with a concentration of dust detected in 5–500 μm imaging (e.g., Lisenfeld et al. 2002; Galliano et al. 2003; Suzuki et al. 2018; Lianou et al. 2014; McCormick et al. 2018). Maps from Spitzer and the Herschel PACS instrument, with resolutions of ~ 2–$10''$, clearly locate warm dust to the position of MIR1/MIR2, also corresponding to the peak reddening $E(B-V)$ inferred from NIR observations (e.g., Pasquali et al. 2011). The coincidence of MIR1 and MIR2 with this knot of dust indicates that the sources are embedded.

4.2 MIR1 and MIR2 as ionizing sources

Tokura et al. (2006) estimate an infrared luminosity of $L_{\rm IR} = (2$–$10) \times 10^7$ L$_\odot$ for MIR1 and $L_{\rm IR} = (4$–$31) \times 10^8$ L$_\odot$ for MIR2, which we have scaled to a distance of $D = 3.4$ Mpc. MIR1 is well-constrained by its detectable radio continuum. While MIR2 lacks such radio emission, it should dominate in the FIR to sub-mm and can thus be constrained by existing low resolution data. Summing the 12-1200 μm global flux densities from SCUBA reported in Lisenfeld et al. (2002) yields a global IR luminosity of $L_{\rm IR} \sim 10^9$ L$_\odot$, putting an upper limit on the combined luminosity of MIR1 and MIR2. Alternatively we can adopt an upper limit of $L_{\rm IR} \sim 4 \times 10^8$ L$_\odot$, the (distance-scaled) dust luminosity over the full central starburst region from SED modelling in Lianou et al. (2014) (see their Table 4). This value is comparable to the optically thick model luminosity of MIR2 from Tokura et al. (2006) and consistent with their interpretation of this mysterious source.

For clusters of less than 5 Myr of age, the implied Lyman continuum rates are then $\log_{10}(N_{\rm LyC}) = 50.6$–$51.3$ for MIR1 and $\log_{10}(N_{\rm LyC}) = 52.0$–$52.8$ for MIR2. MIR2 is comparable to the supernebula in NGC 5253, and thus has a mass of roughly $3 - 5 \times 10^5$ M$_\odot$, and contains roughly 2000 O stars. To be consistent with these implied Lyman continuum rates, MIR1 should have a radio continuum flux of 0.4–2 mJy and MIR2 12–50 mJy at wavelengths of 6 cm. The observed flux for MIR1 is 2 mJy, as expected. However, the flux of MIR2 is < 1 mJy, at least a factor of 10 too low. This suggests that the turnover frequency for the free-free spectrum is higher than 6 cm.

The Brackett emission, detected bright, extended ($\sim 2\rlap{.}''2 \simeq 35$ pc) source Br-MIR1, should follow radio continuum fluxes and similarly bear witness to a lack of ionization in MIR2. Using the observed 6 cm fluxes, we follow Ho et al. (1990) to predict the expected Br α fluxes, and compare to the observed value. Adopting $T_e = 1.5 \times 10^4$ yields expected fluxes of 4×10^{-16} W m^{-2} for MIR1 and $\lesssim 6 \times 10^{-17}$ W m^{-2} for MIR2. The actual observed flux is $F_{\rm Br\,\alpha} = 2 \times 10^{-16}$ W m^{-2} (Table 1). This value is consistent with the total radio-predicted flux of MIR1 and MIR2 after correcting for extinction and considering additional slit loss. MIR2 thus likely contributes $\lesssim 10\%$ of the emission of Br-MIR1, and gas belonging to MIR1 should dominate the line profile (Fig. 4).

Following Tokura et al. (2006) and using higher frequency radio continuum fluxes, we can use the missing radio continuum flux from MIR2 to estimate a turnover frequency, and thus an emission measure, EM $= \int n_e^2 \, d\ell$. If we assume that MIR2 should have 12 mJy of radio flux at
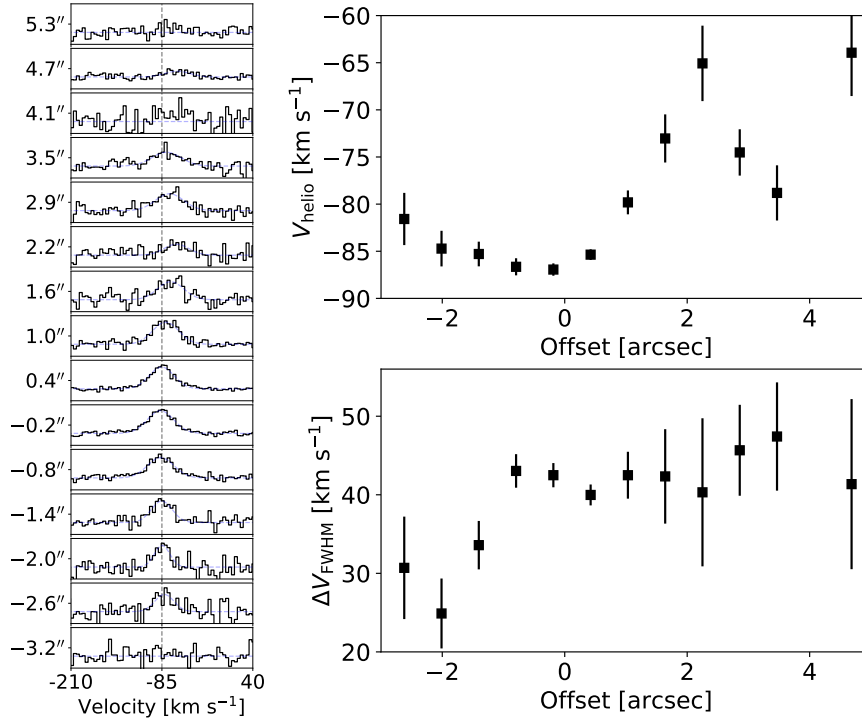
Figure 7. The Br α spectrum as a function of position along the slit (north-south). *Left*) Observed spectrum extracted every $0''6 = 4$ pix along the slit axis (black line) and fit with a Gaussian profile (blue-dashed line) to measure velocity centroid and line width. The vertical black dashed line shows the systemic velocity, $V_{\rm sys} = -85$ km s^{-1}. *Right*) Centroid velocity (top) and line width (bottom) versus position along the slit (offset increases north).

Table 1. Properties of the two Br α sources identified in Fig. 2 and 3.

Source	Offset[a]	$\Delta\theta_{\rm FWHM}$[b]	$F_{\rm tot}[10^{-17}$ W m$^{-2}]$[c]	$V_{\rm hel}$[km s$^{-1}]$[d]	ΔV[km s$^{-1}]$[e]
Br-MIR1	0.0	2.2 ± 0.2	20 ± 4	-85 ± 1	42 ± 2
Br-N	3.1	1.2 ± 0.3	4 ± 1	-73 ± 2	45 ± 5

$F_n/F_{\rm tot}$[f]	$V_{\rm n}$[km s$^{-1}]$[g]	$\Delta V_{\rm n}$[km s$^{-1}]$[h]	$F_b/F_{\rm tot}$[i]	$V_{\rm b}$[km s$^{-1}]$[j]	$\Delta V_{\rm b}$[km s$^{-1}]$[k]
0.55	-85 ± 1	32 ± 3	0.45	-88 ± 3	74 ± 12
....	....	....	....	....	....

[a] Spatial offset (along slit, north is positive) from the brightest source, Br-MIR1 (Fig. 3).
[b] Angular size of source (FWHM) from the best-fit single Gaussian profile to the 1D spatial profile (Fig. 2).   [c] Br α line flux derived from the best-fit model of the 1D spectra (Fig. 3) extracted within a $2''2$ aperture; for Br-MIR1, the total flux of both fit components.
[d] Heliocentric centroid velocity from a single-component fit of the Br α emission (Fig. 3).
[e] Br α velocity line width (FWHM) of the single-component fit to the spectrum.
[f] Fraction of total flux in the narrow component from the best-fit two-component spectrum (Fig. 3).
[g] Heliocentric centroid velocity of the narrow fit component.   [h] Br α velocity line width (FWHM) of the narrow fit component (Fig. 3).   [i] Fraction of total flux in the broad component from the best-fit two-component spectrum (Fig. 3).   [j] Heliocentric centroid velocity of the broad fit component.   [k] Br α velocity line width (FWHM) of the broad fit component.

6 cm but a flux of only 0.2 mJy is observed, since the optical depth goes as $\nu^{-2.1}$ (Draine 2011), the implied turnover frequency is roughly 50 GHz. The emission measure is thus $EM \sim 10^{10}$ cm^{-6} pc. This high emission measure puts MIR2 into the category of hypercompact HII regions. For a uniform density region, assuming a size of 3 pc typical of GCs and NGC 5253 (Turner et al. 2017; Consiglio et al. 2017), this would apply an rms density of $n_e \gtrsim 10^5$ cm^{-3}. Since the ionized gas is probably clumped, and since the supernebula associated with MIR2 probably consists of multiple individual HII regions (Beck 2008; Cohen et al. 2018; Silich et al. 2020), the ionized gas densities are probably higher than 10^5 cm^{-3}.

4.3 Dynamical Constraints

Theoretical work on forming massive clusters have found that a cluster's ability to survive feedback from its first generation of stars and to retain enough gas to form a second stellar generation is closely linked to its initial mass concentration M/R (e.g., Krause et al. 2016; Silich & Tenorio-Tagle 2018; Elmegreen 2018). Using the Br α line width we can estimate the concentration of the clusters powering Br-MIR1, a lower limit which likely traces the lower density gas in MIR1. Observed IR hydrogen recombination line widths result from the convolution of thermal Doppler broadening $\Delta V_{\mathrm{thermal}} = \sqrt{k_B T_e / m_H}$ and non-thermal turbulent broadening due to gravity or feedback. Assuming $T_e = 1.5 \times 10^4$ K, the single-component line width $\Delta V_{\mathrm{obs}} = 42 \pm 2$ km s^{-1} corresponds to a turbulent width $\Delta V_{\mathrm{turb}} = 31 \pm 3$ km s^{-1}, where we have also subtracted the instrumental line width in quadrature. If the turbulent width is solely due to gravity we can estimate the compactness using the virial theorem (MacLaren et al. 1988): $M/R = 190\Delta V_{\mathrm{turb}}^2 \sim 2 \times 10^5$ M$_\odot$ pc^{-1}, assuming a $1/r$ density profile. These values are consistent with kinematic measurements of of SSCs in NGC 5253, II Zw 40, He 2-10, the Antennae (e.g., Henry et al. 2007; Beck et al. 2013, 2015; Turner et al. 2003; Cohen et al. 2018). We note that if we instead use the narrow, broad component line widths of the two-component fit (Fig. 3), we estimate $M/R \sim 10^5$ M$_\odot$ pc^{-1} and $M/R \sim 10^6$ M$_\odot$ pc^{-1}.

The mass concentration and observed size ($R_{cl} \sim 1'' = 16$ pc) imply a cluster mass of $M_{cl} \sim 3 \times 10^6$ M$_\odot$. This is an upper limit to the mass of MIR1, since the radius is unlikely to be 15 pc. A more appropriate mass might be if $R = 3$ pc, a typical globular cluster radius, is assumed, which gives a mass of 6×10^5 M$_\odot$. Indeed, the extinction-corrected ionizing photon luminosity derived above results in a mass of $M_{cl} \sim 3 \times 10^5$ M$_\odot$, which does not include any direct absorption of photons by dust.

5   SUMMARY

Using NIRSPEC we have observed the Br α 4.05 μm emission line across the embedded star-forming region in NGC 1569, at the location of the galaxy's brightest H II region complex and two candidate SSCs MIR1 and MIR2. Presented alongside VLA radio continuum mapping and TEXES [S IV] 10.5 μm spectroscopy, the results give us novel insight into feedback in a potential globular cluster formation site:

(i) The recombination line flux of the H II region complex is dominated by a bright source with size $\Delta\theta \simeq 2''2 = 35$ pc, which we associate with the mid-IR source of Tokura et al. (2006) MIR1 and hence identify as Br-MIR1. Its spatial profile is consistent with the radio continuum mapping and indicates a structure comprising a compact emission peak with a southern shoulder across the position of mid-IR source MIR2. The shoulder suggests a physical link between MIR1 and MIR2.

(ii) The ionized gas line width of the embedded H II region complex is extremely symmetric and narrow, only 40-45 km s^{-1} FWHM, measured for both the Br α and [S IV] lines. This is comparable to Galactic hypercompact H II regions. The flux and line width implies a mass of $\sim 10^5$ within a $R_{cl} \sim 1$ pc cluster. It appears that feedback from the super star clusters is currently ineffective at driving rapid gas dispersal due to their extreme youth and the high density of H II regions within.

(iii) The Br α and radio continuum fluxes of source MIR2 predicted by its MIR continuum (Tokura et al. 2006) are much larger than those observed. The ionized gas appears to be very dense, with EM $\gtrsim 10^{10}$ cm^{-6} pc, such that MIR2 is in the extremely young hypercompact H II region phase.

Clearly NGC 1569's embedded H II region complex, hosting candidate SSCs MIR1 and MIR2, warrants further investigation. New high resolution maps of the dust and gas near these sources will be necessary for constraining their fundamental properties, determining their formation and evolution, and uncovering any physical link between them. In particular MIR2, the more massive SSC, is likely in the earliest phases of formation in which ionization is quenched in extremely dense H II regions around thousands of individual massive stars. Such observational targets are going to be vital in understanding the formation of massive star clusters and their effects on the galaxies in which they reside.

DATA AVAILABILITY

The data underlying this article are publicly available through the Keck Observatory Archive at `https://www2.keck.hawaii.edu/koa/public/koa.php` under Program ID: U048 (PI: J. Turner), along with the NRAO Science Data Archive at `https://archive.nrao.edu/archive/advquery.jsp` under Program ID: AT0227 (PI: J. Turner).

REFERENCES

Bastian N., Lardo C., 2018, ARA&A, 56, 83
Beck S. C., 2008, A&A, 489, 567
Beck S., Turner J., Lacy J., Greathouse T., Lahad O., 2013, ApJ, 767, 53
Beck S., Turner J., Lacy J., Greathouse T., 2015, ApJ, 814, 16
Calzetti D., et al., 2015, ApJ, 811, 75
Clark D. M., Eikenberry S. S., Raines S. N., Gruel N., Elston R., Guzman R., Boreman G., Glenn P. E., 2013, MNRAS, 428, 2290
Cohen D. P., Turner J. L., Consiglio S. M., Martin E. C., Beck S. C., 2018, ApJ, 860, 47

Consiglio S. M., Turner J. L., Beck S., Meier D. S., Silich S., Zhao J.-H., 2017, preprint, (arXiv:1710.10282)

Draine B. T., 2011, ApJ, 732, 100

Elmegreen B. G., 2018, ApJ, 869, 119

Gaia Collaboration et al., 2016, A&A, 595, A1

Gaia Collaboration et al., 2018, A&A, 616, A1

Galliano F., Madden S. C., Jones A. P., Wilson C. D., Bernard J. P., Le Peintre F., 2003, A&A, 407, 159

Gray W. J., Oey M. S., Silich S., Scannapieco E., 2019, ApJ, 887, 161

Greve A., Tarchi A., Hüttemeister S., de Grijs R., van der Hulst J. M., Garrington S. T., Neininger N., 2002, A&A, 381, 825

Grocholski A. J., van der Marel R. P., Aloisi A., Annibali F., Greggio L., Tosi M., 2012, AJ, 143, 117

Henry A. L., Turner J. L., Beck S. C., Crosthwaite L. P., Meier D. S., 2007, AJ, 133, 757

Hindson L., et al., 2018, ApJS, 234, 29

Ho P. T. P., Beck S. C., Turner J. L., 1990, ApJ, 349, 57

Hoare M. G., Kurtz S. E., Lizano S., Keto E., Hofner P., 2007, in Reipurth B., Jewitt D., Keil K., eds, Protostars and Planets V. p. 181 (arXiv:astro-ph/0603560)

Hunter D. A., O'Connell R. W., Gallagher J. S., Smecker-Hane T. A., 2000, AJ, 120, 2383

Johnson M., Hunter D. A., Oh S.-H., Zhang H.-X., Elmegreen B., Brinks E., Tollerud E., Herrmann K., 2012, AJ, 144, 152

Krause M. G. H., Charbonnel C., Bastian N., Diehl R., 2016, A&A, 587, A53

Lacy J. H., Richter M. J., Greathouse T. K., Jaffe D. T., Zhu Q., 2002, PASP, 114, 153

Lianou S., Barmby P., Rémy-Ruyer A., Madden S. C., Galliano F., Lebouteiller V., 2014, MNRAS, 445, 1003

Lisenfeld U., Israel F. P., Stil J. M., Sievers A., 2002, A&A, 382, 860

Lisenfeld U., Wilding T. W., Pooley G. G., Alexand er P., 2004, MNRAS, 349, 1335

MacLaren I., Richardson K. M., Wolfendale A. W., 1988, ApJ, 333, 821

McCormick A., et al., 2018, MNRAS, 477, 699

McLean I. S., et al., 1998, in Fowler A. M., ed., Proc. SPIE Vol. 3354, Infrared Astronomical Instrumentation. pp 566–578, doi:10.1117/12.317283

Meier D. S., Turner J. L., Beck S. C., 2002, AJ, 124, 877

Pasquali A., et al., 2011, AJ, 141, 132

Piotto G., et al., 2015, AJ, 149, 91

Sewilo M., Churchwell E., Kurtz S., Goss W. M., Hofner P., 2004a, ApJ, 605, 285

Sewilo M., Churchwell E., Kurtz S., Goss W. M., Hofner P., 2004b, ApJ, 605, 285

Silich S., Tenorio-Tagle G., 2017, MNRAS, 465, 1375

Silich S., Tenorio-Tagle G., 2018, MNRAS, 478, 5112

Silich S., Tenorio-Tagle G., Martínez-González S., Turner J., 2020, MNRAS, 494, 97

Smith L. J., Crowther P. A., Calzetti D., Sidoli F., 2016, ApJ, 823, 38

Suzuki T., Kaneda H., Onaka T., Yamagishi M., Ishihara D., Kokusho T., Tsuchikawa T., 2018, MNRAS, 477, 3065

Taylor C. L., Hüttemeister S., Klein U., Greve A., 1999, A&A, 349, 424

Tokura D., et al., 2006, ApJ, 648, 355

Turner J. L., 2009, Astrophysics and Space Science Proceedings, 10, 215

Turner J. L., Beck S. C., 2004, ApJ, 602, L85

Turner J. L., Beck S. C., Ho P. T. P., 2000, ApJ, 532, L109

Turner J. L., Beck S. C., Crosthwaite L. P., Larkin J. E., McLean I. S., Meier D. S., 2003, Nature, 423, 621

Turner J. L., Beck S. C., Benford D. J., Consiglio S. M., Ho P. T. P., Kovács A., Meier D. S., Zhao J.-H., 2015, Nature, 519, 331

Turner J. L., Consiglio S. M., Beck S. C., Goss W. M., Ho P. T. P., Meier D. S., Silich S., Zhao J.-H., 2017, ApJ, 846, 73

Waller W. H., 1991, ApJ, 370, 144

Westcott J., Brinks E., Hindson L., Beswick R., Heesen V., 2018, MNRAS, 475, 5116

Westmoquette M. S., Exter K. M., Smith L. J., Gallagher J. S., 2007, MNRAS, 381, 894

This paper has been typeset from a TEX/LATEX file prepared by the author.